HHS Public Access

Author manuscript

Neuroinformatics. Author manuscript; available in PMC 2016 May 19.

Published in final edited form as:

Neuroinformatics. 2015 July ; 13(3): 367–381. doi:10.1007/s12021-015-9264-7.

Segmentation of the Cerebellar Peduncles Using a Random Forest Classifier and a Multi-object Geometric Deformable Model: Application to Spinocerebellar Ataxia Type 6

Chuyang Ye,

Department of Electrical and Computer Engineering, Johns Hopkins University, Baltimore, MD, USA, Tel.: +14435406455

Zhen Yang,

Department of Electrical and Computer Engineering, Johns Hopkins University, Baltimore, MD, USA

Sarah H. Ying, and

Departments of Radiology, Neurology, and Ophthalmology, Johns Hopkins University School of Medicine, Baltimore, MD, USA

Jerry L. Prince

Department of Electrical and Computer Engineering, Johns Hopkins University, Baltimore, MD, USA

Chuyang Ye: cye4@jhu.edu

Abstract

The cerebellar peduncles, comprising the superior cerebellar peduncles (SCPs), the middle cerebellar peduncle (MCP), and the inferior cerebellar peduncles (ICPs), are white matter tracts that connect the cerebellum to other parts of the central nervous system. Methods for automatic segmentation and quantification of the cerebellar peduncles are needed for objectively and efficiently studying their structure and function. Diffusion tensor imaging (DTI) provides key information to support this goal, but it remains challenging because the tensors change dramatically in the decussation of the SCPs (dSCP), the region where the SCPs cross. This paper presents an automatic method for segmenting the cerebellar peduncles, including the dSCP. The method uses volumetric segmentation concepts based on extracted DTI features. The dSCP and noncrossing portions of the peduncles are modeled as separate objects, and are initially classified using a random forest classifier together with the DTI features. To obtain geometrically correct results, a multi-object geometric deformable model is used to refine the random forest classification. The method was evaluated using a leave-one-out cross-validation on five control subjects and four patients with spinocerebellar ataxia type 6 (SCA6). It was then used to evaluate group differences in the peduncles in a population of 32 controls and 11 SCA6 patients. In the SCA6 group, we have observed significant decreases in the volumes of the dSCP and the ICPs and

Information Sharing Statement

The method is available on the Neuroimaging Informatics Tools and Resources Clearinghouse (NITRC) website (http://www.nitrc.org/). The instructions and other details are at http://www.iacl.ece.jhu.edu/Chuyang/CPSeg.

significant increases in the mean diffusivity in the noncrossing SCPs, the MCP, and the ICPs. These results are consistent with a degeneration of the cerebellar peduncles in SCA6 patients.

Keywords

Cerebellar peduncles; Random forest classifier; Multi-object geometric deformable model; Spinocerebellar ataxia type 6

1 Introduction

The cerebellar peduncles are major white matter tracts which communicate information between the cerebellum and other brain regions, including the cerebral cortex and the spinal cord (Sivaswamy et al, 2010). They comprise the superior cerebellar peduncles (SCPs), the middle cerebellar peduncle (MCP), and the inferior cerebellar peduncles (ICPs). An illustration of the structures of the peduncles is shown in Fig. 1, together with the cerebellum and the brainstem. The SCPs are the major efferent pathways that convey the output information from the cerebellum to the midbrain. The SCPs originate primarily from the dentate nuclei and then continue upward toward the brainstem, where the left and right SCPs cross each other in a region known as the decussation of the SCP (dSCP). The fibers then head toward the red nuclei on the opposite side, where some fibers terminate but most continue through to the thalamus (Perrini et al, 2012). The MCP is the largest afferent system of the cerebellum and acts as the afferent pathway from the pons to the cerebellum. It wraps around the pons and ends in the cerebellar cortex (Perrini et al, 2012; Mori et al, 2005). The ICPs contain both afferent and efferent signals and connect the medulla to the cerebellum (Mori et al, 2005).

The cerebellar peduncles play an important role in motor and non-motor control (Nolte, 2002) and are known to be affected by various neurological diseases, including spinocerebellar ataxia (Ying et al, 2009; Murata et al, 1998), schizophrenia (Wang et al, 2003), and multiple system atrophy (Nicoletti et al, 2006). Previous studies on cerebellar peduncle atrophy have used manual delineations of the peduncles on magnetic resonance images (Ying et al, 2009; Murata et al, 1998), which can be subjective and time-consuming. Automatic segmentation of the cerebellar peduncles is therefore a crucial step which will enable larger studies involving more objective, reproducible, and efficient analytic methods.

By capturing the anisotropy of water diffusion in white matter tracts, *diffusion tensor imaging* (DTI) (Le Bihan et al, 2001) provides a noninvasive tool for reconstruction of the cerebellar peduncles. Many algorithms for automatic segmentation of the white matter tracts based on DTI have been proposed. These methods can be grouped into two categories: 1) clustering and labeling of computed fibers (O'Donnell et al, 2006; O'Donnell and Westin, 2007; Maddah et al, 2005, 2008; Wang et al, 2011; Zhang et al, 2008; Lawes et al, 2008; Suarez et al, 2012; Ye et al, 2012) and 2) volumetric segmentation (Bazin et al, 2011; Hao et al, 2014; Awate et al, 2007; Wang and Vemuri, 2005; Lenglet et al, 2006; Ye et al, 2013). Some prior methods have been developed specifically for the cerebellar peduncles. For example, Zhang et al (2008) compute a proximity measure for each pair of computed fibers and then cluster the fibers using a single-linkage algorithm. In Ye et al (2012), a supervised

Gaussian classifier is employed to label the fiber tracts. In Bazin et al (2011), an atlas-based Markov random field is used to segment the cerebellar peduncles volumetrically, and then each voxel is given a label.

None of the existing methods adequately segment the dSCP. In Zhang et al (2008) and Ye et al (2012), for example, the dSCP is entirely missing such that the SCPs pass beyond the red nuclei while never crossing (see Fig. 2(a)). The problem occurs in large part because fiber tracking methods do not correctly track the separate tracts through the dSCP. Fiber tracking methods that resolve crossing fibers have been reported (Qazi et al, 2009; Malcolm et al, 2010; Peled et al, 2006; Landman et al, 2012; Ramirez-Manzanares et al, 2007; Behrens et al, 2007; Zhou et al, 2014; Michailovich et al, 2011), but none of them have yet demonstrated the ability to resolve the dSCP. Although imaging methods that acquire more diffusion information—e.g., high angular resolution diffusion imaging (HARDI) (Tuch et al, 2002) and diffusion spectrum imaging (DSI) (Wedeen et al, 2005)—can potentially enable detailed evaluation of the crossing fibers in the dSCP, they take a much longer imaging time than standard DTI, which makes them less practical for clinical use. In addition, with the large number of existing and ongoing DTI acquisitions, scientific studies on the cerebellar peduncles using DTI are still widely performed (Cavallari et al, 2013; Clemm von Hohenberg et al, 2013; Hanaie et al, 2013; Hüttlova et al, 2014; Wang et al, 2014; Buijink et al, 2014; Ojemann et al, 2013). Therefore, development of better cerebellar peduncle segmentation methods on DTI remains an important technical goal.

One way to avoid using fiber tracking in tract segmentation is to directly segment the tracts by labeling the voxels based on features derived from DTI. For example, the DOTS method reported in Bazin et al (2011) explicitly models crossing regions and attempts to find them by matching their features near where they are expected to be found according to an atlas registered to the subject. Unfortunately, because of the small size of the dSCP, DOTS is unable to register the feature atlas close enough to find the dSCP in test subjects. An improvement to DOTS reported in Ye et al (2013) incorporates the linear Westin index (Westin et al, 1997) as an additional feature, but this is still insufficient to provide a robust initialization and segmentation of the dSCP.

In this paper, we propose an automatic method to volumetrically segment the cerebellar peduncles including the dSCP. The method models the dSCP, the noncrossing portions of the SCPs, the MCP, and the ICPs as separate objects based on the observation that the diffusion properties in these regions, including the primary eigenvectors (PEVs) of the tensors and the Westin indices describing the shape of the tensors (Westin et al, 1997), exhibit certain homogeneous properties. These features, together with spatial position information, are used to train a random forest classifier (RFC) (Breiman, 2001) from manual delineations. The RFC is then used on new subjects to segment and label the peduncles. Because smoothness is not enforced in the RFC, a further segmentation step is carried out using a multi-object geometric deformable model (MGDM) (Bogovic et al, 2013), which refines and smooths out the boundaries. An example of the proposed segmentation, depicting the SCPs that decussate, is shown in Fig. 2(b). Note that in this work, we do not include the SCPs beyond the decussation because they cannot be well identified on DTI (Mori et al, 2005).

To show that the algorithm is scientifically useful, we studied differences between healthy controls and patients with a genetically defined cerebellar disease, spinocerebellar ataxia type 6 (SCA6). SCA6 is an autosomal dominant cerebellar ataxia and is characterized by progressive problems with movement (Murata et al, 1998). Patients with SCA6 can experience discoordination, speech difficulties, and involuntary eye movements (Sinke et al, 2001). By studying the relationship between the cerebellar peduncles and SCA6, a better understanding of the disease with respect to anatomical changes can be obtained. Although previous studies have partially explored this relationship, they were applied in an indirect way by either measuring the diameter of the midbrain at the SCP level (Murata et al, 1998), or manually delineating regions of interest (ROIs) for analysis (Ying et al, 2009). In this work, we automatically segmented the cerebellar peduncles of controls and SCA6 patients. Then the volume, fractional anisotropy (FA), and mean diffusivity (MD) of each peduncle were quantified and compared between the two groups.

The rest of the paper is organized as follows. Section 2 provides our cerebellar peduncle segmentation method, including the random forest classification and MGDM refinement. It also describes the parameter settings and the data acquisition used in this work. In Section 3, validations of the proposed method including controls and patients with SCA6 are presented with qualitative evaluation and quantitative measurement. An experiment that involves a larger data set and compares the statistics of controls and SCA6 patients is also presented. The results of the experiments and the limitations and potential extensions of the proposed method are discussed in Section 4. Finally, Section 5 summarizes and concludes this paper.

2 Materials and methods

2.1 Random Forest Classification of the Cerebellar Peduncles

An RFC is used to label each voxel, providing an initial estimation of the locations of the cerebellar peduncles. The RFC, which is trained by manual delineations of the peduncles, determines the classification using characteristic features including diffusion properties and spatial location information.

2.1.1 RFC—An RFC is a supervised classifier that is composed of a number of decision trees. In this work, the RFC is implemented using the WEKA software (Hall et al, 2009) (http://www.cs.waikato.ac.nz/ml/index.html). Each tree is constructed based on a bootstrap sample randomly sampled with replacement from the training set, where the bootstrap sample has the same size as the training set (Breiman, 2001). At each node of a tree, a subset of features is selected randomly and the split is determined based on the selected features (without linear combination), i.e., the “Forest-RI” strategy in Breiman (2001). Specifically, a classification and regression tree (CART) (Breiman et al, 1984) methodology for growing trees is used in the RFC, where the split that results in the greatest decrease in the Gini impurity is selected at each node (Breiman et al, 1984). Splitting is terminated when no impurity decrease can be achieved, or some pre-defined termination criterion, such as the maximum depth of the tree, is reached. For each test sample, each tree provides a label by the terminal node where the sample ends. Using the results from all trees, a membership function m_i indicating the likelihood of the sample belonging to class i can be calculated as

$m_i = N_i/N$, where N_i is the number of the trees predicting class i, and N is the total number of the trees in the forest. The class that corresponds to the maximum membership is selected as the label. This process yields both an estimated label and membership functions for all the labels which will be later used in the MGDM segmentation. In this work, seven labels are used: left noncrossing SCP (lSCP), right noncrossing SCP (rSCP), dSCP, MCP, left ICP (lICP), right ICP (rICP), and background (BG). Note that the noncrossing SCPs and the dSCP are different objects.

2.1.2 Features in the RFC—To apply the RFC, features must be extracted from the images and input into the classifier. Here, based on the observation that the cerebellar peduncles can be identified using the diffusion properties and spatial location, we use the PEV, the Westin indices (Westin et al, 1997), and a registered template to provide features.

When there is one primary diffusion direction, the PEV provides a good approximation of the direction (Mori et al, 2005). Therefore, the PEV is a useful feature indicating the existence of tracts where there is no overlap. However, the PEV has bidirectional ambiguity; for example, (−1, 0, 0) and (1, 0, 0) represent the same PEV. Therefore, we map the PEV $u = (u_1, u_2, u_3)$ into a 5D Knutsson space as follows (Knutsson, 1985):

$$\begin{aligned} \boldsymbol{v} &= (v_1, v_2, v_3, v_4, v_5) \\ &= \frac{1}{\|\boldsymbol{u}\|}(u_1^2 - u_2^2, 2u_1u_2, 2u_1u_3, 2u_2u_3, \frac{1}{\sqrt{3}}(2u_3^2 - u_1^2 - u_2^2)). \end{aligned} \quad (1)$$

This mapping eliminates the directional ambiguity, and the resulting 5D Knutsson vector v serves as a feature in the RFC. An example of the Knutsson vector focused on the cerebellar peduncles in two axial slices is shown in Fig. 3(a). The locations of the cerebellar peduncles are indicated within these slices and also shown as labels in Fig. 3(b).

Although the PEV is a useful feature for the identification of tracts, it does not give useful information on whether fibers cross in a region. Thus, additional information for differentiation of noncrossing and crossing regions is required. The Westin indices can be used for this purpose (Westin et al, 1997). The linear index C_l, the planar index C_p, and the spherical index C_s describe how linear, planar, and spherical, a tensor is shaped, respectively. Let $\lambda_1 \geq \lambda_2 \geq \lambda_3 \geq 0$ be the eigenvalues of the diffusion tensor; the Westin indices are calculated as follows (Westin et al, 1997):

$$C_l = \frac{\lambda_1 - \lambda_2}{\lambda_1+\lambda_2+\lambda_3}, \quad C_p = \frac{2(\lambda_2 - \lambda_3)}{\lambda_1+\lambda_2+\lambda_3}, \text{ and } C_s = \frac{3\lambda_3}{\lambda_1+\lambda_2+\lambda_3}. \quad (2)$$

Note that $0 \leq C_l, C_p, C_s \leq 1$ and $C_l + C_p + C_s = 1$. An example of the Westin indices is provided in Fig. 3(c). When there is one primary diffusion direction, the tensor is linear-shaped and therefore high C_l values are expected. In the dSCP, the tensor is planar because it has crossing fibers, and therefore C_p increases and C_l drops. In isotropic areas, the tensor is spherical, and therefore C_s is large. Therefore, the Westin indices $\boldsymbol{C} = (C_l, C_p, C_s)$ are included as features to differentiate the cases of noncrossing tracts, crossing tracts, and isotropic areas.

An initial estimate of the spatial locations of all the cerebellar peduncles including the dSCP can be provided by registering a template to the subject to be segmented. We generated such a template by manual segmentation of a single subject. After experimentation, we determined that SyN registration (Avants et al, 2008) using the linear Westin index provides a reliable registration of the template to the target subject, where the mean square difference is selected as the similarity measure. To incorporate the information provided by SyN registration into the RFC, signed distance functions (SDFs), φ_{lSCP}, φ_{rSCP}, φ_{dSCP}, φ_{MCP}, φ_{lICP}, and φ_{rICP} are calculated from these transformed lSCP, rSCP, dSCP, MCP, lICP, and rICP labels, respectively. We refer to the SDFs as *spatial information* because these features provide information on the spatial locations of the cerebellar peduncles. These distance maps $\varphi = (\varphi_{\mathrm{lSCP}}, \varphi_{\mathrm{rSCP}}, \varphi_{\mathrm{dSCP}}, \varphi_{\mathrm{MCP}}, \varphi_{\mathrm{lICP}}, \varphi_{\mathrm{rICP}})$ can indicate how far a voxel of the target subject is from the registered labels. Since the tracts should be close to the corresponding registered labels, lower values on a certain SDF could indicate higher possibility of the voxel belonging to the tract.

For each voxel at (*x, y, z*), we also supplement the SDFs with relative positions to the centers of the registered labels as additional spatial features:

$$\boldsymbol{x}_i=(x_i,y_i,z_i)=(x-\overline{x}_i,y-\overline{y}_i,z-\overline{z}_i), i\in\{\mathrm{lSCP},\mathrm{rSCP},\mathrm{dSCP},\mathrm{MCP},\mathrm{lICP},\mathrm{rICP}\}, \quad (3)$$

where ($\overline{x}_i$, $\overline{y}_i$, $\overline{z}_i$) is the center of the registered labels. The relative positions

$$\boldsymbol{x}=(\boldsymbol{x}_{\mathrm{lSCP}},\boldsymbol{x}_{\mathrm{rSCP}},\boldsymbol{x}_{\mathrm{dSCP}},\boldsymbol{x}_{\mathrm{MCP}},\boldsymbol{x}_{\mathrm{lICP}},\boldsymbol{x}_{\mathrm{rICP}}) \quad (4)$$

give more detailed relationships between voxels and transformed templates.

In summary, the final feature vector $\boldsymbol{f}$ to be used in the RFC is a 32-dimensional vector composed of the Knutsson vector $\boldsymbol{v}$, the Westin indices $\boldsymbol{C}$, and the spatial information from the SDFs φ, and the relative positions $\boldsymbol{x}$, i.e.,

$$\boldsymbol{f}=(\boldsymbol{v},\boldsymbol{C},\phi,\boldsymbol{x}). \quad (5)$$

2.1.3 Manual Delineations—To train the RFC, manual delineations of the cerebellar peduncles were made using a PEV edge map (Fan et al, 2010) and the linear Westin index. The PEV edge map is computed by first estimating the gradient matrix **G** of the 5D Knutsson vector with a finite difference operator (Fan et al, 2010):

$$\mathbf{G}=\begin{pmatrix} \frac{\partial v_1}{\partial x} & \frac{\partial v_1}{\partial y} & \frac{\partial v_1}{\partial z} \\ \frac{\partial v_2}{\partial x} & \frac{\partial v_2}{\partial y} & \frac{\partial v_2}{\partial z} \\ \frac{\partial v_3}{\partial x} & \frac{\partial v_3}{\partial y} & \frac{\partial v_3}{\partial z} \\ \frac{\partial v_4}{\partial x} & \frac{\partial v_4}{\partial y} & \frac{\partial v_4}{\partial z} \\ \frac{\partial v_5}{\partial x} & \frac{\partial v_5}{\partial y} & \frac{\partial v_5}{\partial z} \end{pmatrix}. \quad (6)$$

Then the Frobenius norm can be calculated to obtain the edge map (Fan et al, 2010):

$$\|\mathbf{G}\|_F = \sqrt{\sum_{j=1}^{3}\sum_{i=1}^{5} G_{ij}^2}. \quad (7)$$

On the PEV edge map, the PEVs inside a tract are homogeneous and appear as dark regions; at the tract boundaries, the PEVs are different from their neighbors and appear as bright edges (see Fig. 4). Therefore, the PEV edge map contributes to the identification of the tracts for human raters. In addition, the noncrossing tracts have higher C_l values and crossing tracts have lower C_l values, which makes the C_l map a useful feature for tract delineation. In practice, these two maps are sufficient for manual determination of the cerebellar peduncles. Fig. 4 gives an example of the manual delineation and its relationship with the PEV edge map and the C_l map.

2.2 MGDM Segmentation

The RFC provides an initial classification of the cerebellar peduncles, but we still have two problems to contend with. First, the RFC applies to each voxel independently, which potentially leaves objects disconnected or highly irregular. Second, the RFC training may have unbalanced samples (where majority classes tend to be favored in RFC decisions), which will produce a bias in the sizes or positions of segmented objects. We therefore use MGDM (Bogovic et al, 2013) as a second stage in order to provide both spatial smoothness and additional fidelity to the data.

2.2.1 MGDM—MGDM is a framework for multiple object segmentation (Bogovic et al, 2013). It efficiently evolves objects using a decomposition of the signed distance functions of all objects, and prevents overlaps and gaps between objects. The conventional speed functions that are used in geometric deformable models (Caselles et al, 1997; Xu et al, 2000) can be applied in MGDM, and MGDM also enables users to use different speed functions on the boundaries between different object pairs. Let $\varphi_{i,j}$ be the level set function for the boundary between object i and j. Then its evolution can be written as:

$$\frac{\partial \phi_{i,j}}{\partial t} + f_{\text{reg}:i,j}|\nabla \phi_{i,j}| + \boldsymbol{f}_{\text{adv}:i,j} \cdot \nabla \phi_{i,j} = \varepsilon \kappa |\nabla \phi_{i,j}|, \quad (8)$$

where $f_{\text{reg}:i,j}$ represents a region speed, $\boldsymbol{f}_{\text{adv}:i,j}$ stands for an advection speed, and κ is a curvature speed. As with any deformable model, MGDM works best if initialized close to the final configuration. Therefore, our RFC segmentation result forms the initialization for MGDM. Using this framework, we can design the speed functions for specific boundaries to refine the RFC segmentation.

2.2.2 Speed Design of MGDM Smoothing—To preserve smoothness, a curvature speed on each boundary is used in MGDM. Using the membership functions from the RFC output, region speeds are also specified. A region speed shrinks or expands the boundary according to the membership functions and prevents the shrinkage caused by the curvature speed so that the boundaries will not deviate far from the RFC result. Region speeds can also correct bias in the RFC. Since the number of background voxels exceeds those of the tracts and the ratio can range from the scale of 10:1 to 1000:1, depending on which peduncle it is,

the RFC results can be biased. For example, a voxel belonging to the cerebellar peduncles can have a relatively high membership value of the true label, yet it is exceeded by an even higher background membership value. By choosing thresholds of the membership in the region speeds, a compensation for the RFC bias can be achieved.

Specifically, the region speed on each boundary is designed as follows:

$$\begin{cases} f_{\text{reg:}i,\text{BG}} = \alpha(m_i - t_i), & i \neq \text{BG} \\ f_{\text{reg:}i,j} = \alpha(m_i - m_j), & i, j \neq \text{BG} \end{cases}. \quad (9)$$

Here α is a weighting constant, t_i is a thresholding constant for tract i, and m_i represents the corresponding membership computed from the RFC. The constant t_i replaces the background membership for the RFC bias compensation, and is determined empirically. In practice, this replacement achieves more accurate results and prevents the background from being overestimated.

2.3 Parameter Settings

In the RFC, 100 trees were constructed and at each tree node five features were randomly sampled during traning. No constraint on the depth of the tree was used. For other settings in the WEKA software, default values were used. To save computational time and memory in the RFC training and test phase, only voxels that are within a certain distance to any of the transformed labels on the registered template were considered. The distance was set to 10 mm to include all the possible voxels of the cerebellar peduncles. In MGDM, the parameters were chosen empirically, where $\alpha = 0.5$, $\varepsilon = 0.05$, $t_i = 0.3$ ($i \neq$ MCP), and $t_i = 0.375$ ($i =$ MCP).

2.4 Data Acquisition and Preprocessing

Two DTI data sets were used in this work, and they are whole-head acquisitions. In the first data set, there are nine subjects (five controls and four patients with SCA6); in the second data set, there are 43 subjects (32 controls and 11 SCA6 patients) that are different from the subjects in the first data set. The first data set was used for the validation of the proposed method and the second data set was used to study group differences between controls and SCA6 patients.

Diffusion weighted images (DWIs) were acquired using a multi-slice, single-shot EPI sequence on a 3T MR scanner (Intera, Philips Medical Systems, Netherlands). The sequence in the first and second data set consist of 32 and 30 gradient directions, respectively, and one $b0$ image. The b-value is 700 s/mm^2. The original in-plane resolution of the two data sets is 2.2 mm × 2.2 mm, with a matrix size of 96 × 96; and the original slice thickness of the two data sets is 2.2 mm with 65 slices acquired. The scanner resampled the slices and generated the output resolution of 0.828 mm × 0.828 mm × 2.2 mm, where the in-plane matrix size is 256 × 256. Then we isotropically resampled the DWIs, where the resolutions of the first and the second data set are 1 mm and 0.828 mm isotropic, respectively. Finally, diffusion tensors were computed using CATNAP (Landman et al, 2007) in the JIST software (Lucas et al, 2010).

3 Results

3.1 Validation

A leave-one-out cross-validation was performed on the nine subjects in the first data set. Manual delineations of the cerebellar peduncles including the dSCP were made on these subjects. For each test subject, the other eight subjects were used in the training phase. Both control subjects and patients with SCA6 were included in the training. Our experiments were performed on a 12-core Linux machine. The feature extraction took around 30 minutes for each training or test subject, of which the SyN registration took around 20 minutes. The training phase with already extracted features took around two hours on average.

In training an RFC, a measure of the relative importance of each feature called *variable importance* (Breiman, 2001) can be computed. The variable importance measures the mean decrease in classification accuracy after permuting the feature over all the trees (Breiman, 2001). In this experiment, the patterns of the variable importance are similar across the subjects. The means and standard deviations of the variable importance of the elements in the feature vector are shown in Fig. 5. The SDF of the MCP and the linear Westin index have much higher importance than the other features.

After training, test data were segmented as proposed. The RFC step with extracted features took around two minutes, and the MGDM step took around seven minutes. An example of the 3D rendering of the segmentation result is displayed in an oblique view in Fig. 6(a), where the noncrossing and crossing SCPs are combined to get the complete left and right SCPs. Examples of the cross sections of the segmentation result overlaid on the FA map are also given on different slices and compared with the manual delineations in Figs. 6(b) and 6(c). The first axial slice shows a cut through the brainstem where the SCPs decussate, and the second slice shows a cut through the cerebellum where all the cerebellar peduncles are visible. It can be seen that the proposed segmentation method is able to correctly localize the cerebellar peduncles.

To quantitatively evaluate the segmentation accuracy of the proposed method, the Dice coefficients (Dice, 1945) and average surface distances (ASDs) between the segmentation results and manual delineations were computed, and they are listed in Tables 1 and 2, respectively. The numbers are also listed for the RFC initialization to show the improvement of MGDM over RFC alone. For convenience, in the tables, the intermediate RFC result and the final segmentation after MGDM refinement are called “RFC” and “RFC + MGDM”, respectively.

Since no existing method provides a comparison of the segmentation of cerebellar peduncles including the dSCP, and volumetric delineations of the cerebellar peduncles of the subjects are available, we compared our result with two registration-based methods. Each subject was segmented by the two registration-based methods using a leave-one-out cross-validation as well. For the first comparison method, we used the SyN registration algorithm (Avants et al, 2008) to map the training delineations to the test target, using the C_l images and mean square difference as the similarity measure. The C_l images were chosen over the FA maps because they provide better contrast for the tracts. Then spatial STAPLE (Asman and

Landman, 2012) was used as the voting scheme. Spatial STAPLE achieves better label fusion than the STAPLE algorithm (Warfield et al, 2004) by incorporating spatially varying rater performance. For the second comparison method, we applied the tensor-based registration method implemented in DTI-TK (Zhang et al, 2007) to map the training delineations to the test target using the diffusion tensor. Then spatial STAPLE (Asman and Landman, 2012) was also used to provide the final segmentation. The two comparison methods are referred to as "SyN + s-STAPLE" and "DTI-TK + s-STAPLE", respectively. The corresponding Dice coefficients and the ASDs are given in Tables 1 and 2. In our experiments, for each test subject, eight registrations must be performed, and each registration took around 20 minutes for both SyN and DTI-TK. Spatial STAPLE took around 2 minutes for each test subject.

The final segmentation of our method is compared with our intermediate RFC result, the SyN + s-STAPLE result, and the DTI-TK + s-STAPLE result. To show the statistical significance of the performance difference, the paired Student's *t*-test and Wilcoxon signed-rank test were performed with respect to the Dice coefficients and ASDs, respectively. The *p*-values are shown in Tables 3 and 4.

To better understand the implications of these experimental results, we first study the difference between RFC and RFC + MGDM results. It can be seen from Table 1 that the proposed method (RFC + MGDM) improves over the RFC results and has mean Dice coefficients ranging from 0.720 to 0.850, a range which is generally thought to be acceptable, especially for small white matter tracts (Awate et al, 2007; Oishi et al, 2011). In Table 2, we can see that the mean ASDs of the proposed intermediate RFC segmentation and final RFC + MGDM segmentation are in the range of 0.472 mm to 0.755 mm and 0.335 mm to 0.697 mm, respectively. Compared to RFC results, the final segmentation (RFC+MGDM) has higher mean Dice coefficients and lower mean ASDs for all the structures, showing the improvement of using MGDM. The improvement of the lICP and rICP segmentation is significant in terms of both Dice coefficients and ASDs in both statistical tests (see Tables 3 and 4).

We now turn to the comparisons of our method (RFC + MGDM) with the two multi-atlas registration-based methods. In Tables 1 and 2, for all the structures, the mean Dice coefficients of the final results of the proposed method are higher than the two competing methods, and the mean ASDs of the proposed method are lower than the two competing methods. With respect to the Dice coefficients, in both statistical tests (see Table 3), the proposed method performs better than SyN + s-STAPLE with significance for the lSCP, the rSCP, the dSCP, and the lICP; the proposed method also shows significantly better performance than DTI-TK + s-STAPLE for the lSCP, the rSCP, the dSCP, and the MCP. With respect to the ASDs, in the paired Student's test (see Table 4), the proposed method better segments the lSCP, the rSCP, and the dSCP than SyN + s-STAPLE with significance, and better segments the lSCP and the dSCP than DTI-TK + s-STAPLE with significance; in the Wilcoxon signed-rank test (see Table 4), the proposed method better segments the lSCP, the rSCP, and the dSCP than SyN + s-STAPLE and DTI-TK + s-STAPLE with significance.

3.2 Application to SCA6

The proposed method was next applied on the second data set which contains 32 controls and 11 patients. All the data in the first smaller data set were included in the training phase and were not used in the testing phase.

Tract volumes, average FAs, and average MDs of the segmented cerebellar peduncles were calculated. The values were corrected using a general linear model to remove the confounding effects of age and sex using the method in Friston et al (1994). These corrected numbers were then analyzed with a Student's *t*-test and a Wilcoxon rank-sum test for comparison between the two groups. The corrected statistics are shown in the box plots in Fig. 7, where structures with significant differences observed in both the Student's *t*-test and the Wilcoxon rank-sum test are indicated. The *p*-values in the two tests are listed in Table 5. Significant decreases in the volumes of the dSCP, the lICP, and the rICP are observed in the SCA6 group in both statistical tests. Although a significant FA increase in the lICP is observed in the SCA6 group in the Wilcoxon rank-sum test, no significant FA changes in both statistical tests are found for any tract. The MD is observed to be increasing with statistical significance in the lSCP, the rSCP, the MCP, the lICP, and the rICP in the SCA6 group in both statistical tests.

4 Discussion

4.1 Interpretation of the Results

In training the RFC, the high variable importance of φ_{MCP} is probably because the number of MCP voxels is much larger than those of the other peduncles. The high variable importance of C_l is consistent with the fact that manual delineations are based, in part, on the C_l map and also because C_l is high for noncrossing white matter tracts, which is largely what is being segmented.

In the cross-validation study, the ICPs have worse mean Dice coefficients and ASDs than the other structures. This could be because the ICPs extend out of the cerebellum into the spinal cord and can be influenced by the field of view (FOV) of the DWIs.

The measurement of the Dice coefficients and ASDs and the statistical tests indicate that the proposed final results (RFC + MGDM) achieve more accurate segmentation than the intermediate RFC. These results also show the superiority of the proposed algorithm to the two multi-atlas registration-based methods. Note that for the dSCP, the proposed method improves the mean Dice coefficient over SyN + s-STAPLE and DTI-TK + s-STAPLE by 0.092 (13.2%) and 0.125 (18.8%), respectively, and improves the mean ASD over SyN + s-STAPLE and DTI-TK + s-STAPLE by 0.196 mm (36.9%) and 0.204 mm (37.8%), respectively. The improvement of the dSCP segmentation is larger than those of the segmentation of the other noncrossing structures. Moreover, this improvement is significant in both statistical tests.

In the second experiment that studies the group differences between controls and SCA6 patients, the significant decreases in the volumes of the dSCP, the lSCP, and the rICP in the SCA6 group reveal atrophy of the cerebellar peduncles. Note that the volumes of the

noncrossing SCPs do not demonstrate significant differences, which emphasizes the importance of segmenting the crossing regions. In the comparison of FA values, it is worth noting that the mean FAs in the ICPs of the SCA6 group tend to be higher than those in the control group. This could be a result of the ICP volume decrease, where the regions with lower FA near the tract boundaries are more affected than the regions with higher FA close to the centerline of the tract. The ICPs with lower FA atrophy more while the ICPs with higher FA are better preserved, causing the average FA in the ICPs to increase. Furthermore, the MD is observed to be increasing significantly in the lSCP, the rSCP, the MCP, the lICP, and the rICP in the SCA6 group. The MD increase can be possibly due to the degeneration of the neural tracts, which could lead to reduction of cells that constrain water and therefore higher diffusion. Thus the increasing MD in these tracts is also a possible sign of their degeneration.

4.2 Limitations and Extensions

For the SCP, we have focused on the dSCP and the noncrossing portions below the dSCP. The boundary of the SCP beyond the dSCP is quite ambiguous on the PEV edge map and the C_J map which we use for delineation. The manual delineations of this part of the SCPs involve a large amount of speculation, and therefore it is not included in this work. Despite the exclusion, the segmentation of the dSCP and the SCP below the dSCP is able to reveal anatomical differences between groups, as shown in the results, and therefore we believe the proposed method is valuable for scientific studies.

Currently, the features used in the RFC are based on the quantities calculated from the single tensor model. It is also possible to use the features from multi-tensor models which estimate multiple fiber directions in a voxel. For example, if a two-tensor model is used, such as Behrens et al (2007), the 5D Knutsson map can also be calculated for the two directions respectively. Similarly, the proposed method can also be combined with HARDI and DSI, where multiple fiber directions can be estimated using constrained spherical deconvolution (Tournier et al, 2007) or q-ball reconstruction with the spherical harmonic basis (Hess et al, 2006) on HARDI, and local maximum method (Hagmann et al, 2007) on DSI. One practical issue may be the order of the multiple directions. When the contributions of the fiber directions are close, the order may be influenced by noise, which causes incorrect feature correspondence. Besides the directional information, scalar quantities such as mixture fractions (Behrens et al, 2007; Landman et al, 2012) and generalized FA (Tuch, 2004) can also be included to aid classification.

The proposed method segments the structure of the cerebellar peduncles. It is also possible to extend it as a general tract segmentation method. For a general set of tracts, the noncrossing and crossing regions need to be identified manually using the C_J and the Knutsson edge map on training subjects. Features can then be calculated to train the RFC. The quality of the manual delineations and the required number of training data will depend on the variability of the tracts of interest, and the manual delineations could take a large amount of time when the tracts have complex structures.

We performed a preliminary study that shows the potential application of the proposed method to the study of cerebellar ataxia. However, the measurement of FA and MD is based

on the single tensor and could have limitations. For example, the FA in crossing regions may cause misleading interpretation because the values can be influenced by tract integrity and/or fiber crossing. Also, the study currently uses measurements calculated in the whole tract volume, but it can be extended to more detailed analysis of the tracts. For example, Yushkevich et al (2008) use medial representations of tracts and enable statistical analysis in a shape-based coordinate system, where detailed information with respect to spatial location can also be analyzed.

Another issue that should be noted in the proposed work is the partial volume effect (PVE), especially with the dSCP since it is very small. To quantitatively evaluate the level of PVE, using the data set in Section 3.2, for each structure we calculated the ratio of the boundary voxels to the total voxels to represent the partial volume fraction. Because the volumes are significantly different for the dSCP and ICPs between the control and SCA6 group, the partial volume fraction was computed separately for the two groups. The means and standard deviations are listed in Table 6. It can be observed that the partial volume fraction is smaller for the MCP, which is a larger structure, and larger for the dSCP, which is a smaller structure. Also, the partial volume fraction is more different between the control and SCA6 group for the dSCP and ICPs than the other structures, which is consistent with the significantly different volumes of the dSCP and ICPs between the control and SCA6 group. The quantities (volume, FA, and MD) calculated from the segmentation could be affected by PVE, and these values by themselves should be interpreted with care. Using a large number of subjects could decrease the variance of statistics due to PVE, yet the results could still be biased. However, the method can still be used to reveal group differences. For example, in the study between controls and SCA6 patients, we have observed significant anatomical differences between patients and healthy controls, despite the presence of PVE.

5 Summary and Conclusion

In this paper, we have proposed an automatic method for segmenting the cerebellar peduncles including the decussation of the SCPs, which is nearly always missing in previous studies. Like the noncrossing cerebellar peduncles, the dSCP is modeled explicitly as a single class. An RFC is used to classify the voxels based on the PEVs, the Westin indices, and spatial information. The RFC result is further refined by MGDM segmentation to confer smoothness and compensate for possible bias due to unbalanced samples.

A leave-one-out cross-validation was carried out for qualitative and quantitative evaluation of the method. The Dice coefficients and average surface distances were calculated. Results on nine subjects indicate that the method is able to resolve the crossing of the SCPs and accurately segment the cerebellar peduncles. Furthermore, the proposed method outperforms two registration-based methods.

Experiments on a larger data set were performed to show that the method is useful for scientific studies. Results indicate that the volumes of the dSCP, the lICP, and the rICP decrease with statistical significance in the SCA6 group. The changes involving the dSCP also emphasizes the importance of the ability to identify the decussation. Furthermore, the mean MD values in non-crossing SCP regions, the MCP, and the ICPs are significantly

larger in the SCA6 group, which is also a possible indicator of tract degeneration. These findings are consistent with the degeneration of the cerebellar peduncles in SCA6 patients and show the benefit of applying the proposed method for scientific studies.

Acknowledgments

This work is supported by NIH/NINDS 5R01NS056307-08 and the China Scholarship Council.

References

Asman AJ, Landman BA. Formulating spatially varying performance in the statistical fusion framework. IEEE Transactions on Medical Imaging. 2012; 31(6):1326–1336. [PubMed: 22438513]

Avants BB, Epstein CL, Grossman M, Gee JC. Symmetric diffeomorphic image registration with cross-correlation: evaluating automated labeling of elderly and neurodegenerative brain. Medical Image Analysis. 2008; 12(1):26–41. [PubMed: 17659998]

Awate SP, Zhang H, Gee JC. A fuzzy, nonparametric segmentation framework for DTI and MRI analysis: With applications to DTI-tract extraction. IEEE Transactions on Medical Imaging. 2007; 26(11):1525–1536. [PubMed: 18041267]

Bazin PL, Ye C, Bogovic JA, Shiee N, Reich DS, Prince JL, Pham DL. Direct segmentation of the major white matter tracts in diffusion tensor images. NeuroImage. 2011; 58(2):458–468. DOI: 10.1016/j.neuroimage.2011.06.020 [PubMed: 21718790]

Behrens TEJ, Berg HJ, Jbabdi S, Rushworth MFS, Woolrich MW. Probabilistic diffusion tractography with multiple fibre orientations: What can we gain? NeuroImage. 2007; 34(1):144–155. [PubMed: 17070705]

Bogovic JA, Prince JL, Bazin PL. A multiple object geometric deformable model for image segmentation. Computer Vision and Image Understanding. 2013; 117(2):145–157. DOI: 10.1016/j.cviu.2012.10.006 [PubMed: 23316110]

Breiman L. Random forests. Machine Learning. 2001; 45(1):5–32.

Breiman, L.; Friedman, J.; Stone, CJ.; Olshen, RA. Classification and regression trees. CRC press; 1984.

Buijink AW, Caan MW, Contarino MF, Schuurman PR, van den Munckhof P, de Bie RM, Olabarriaga SD, Speelman JD, van Rootselaar AF. Structural changes in cerebellar outflow tracts after thalamotomy in essential tremor. Parkinsonism & Related Disorders. 2014; 20(5):554–557. DOI http://dx.doi.org/10.1016/j.parkreldis.2014.02.020. [PubMed: 24637119]

Caselles V, Kimmel R, Sapiro G. Geodesic active contours. International Journal of Computer Vision. 1997; 22(1):61–79.

Cavallari M, Moscufo N, Skudlarski P, Meier D, Panzer VP, Pearlson GD, White WB, Wolfson L, Guttmann CR. Mobility impairment is associated with reduced microstructural integrity of the inferior and superior cerebellar peduncles in elderly with no clinical signs of cerebellar dysfunction. NeuroImage: Clinical. 2013; 2(0):332–340. [PubMed: 24179787]

Dice LR. Measures of the amount of ecologic association between species. Ecology. 1945; 26(3):297–302.

Fan X, Thompson M, Bogovic JA, Bazin PL, Prince JL. A novel contrast for DTI visualization for thalamus delineation. Proceedings of SPIE Medical Imaging. 2010; 7625

Friston KJ, Holmes AP, Worsley KJ, Poline JP, Frith CD, Frackowiak RS. Statistical parametric maps in functional imaging: a general linear approach. Human Brain Mapping. 1994; 2(4):189–210.

Hagmann P, Kurant M, Gigandet X, Thiran P, Wedeen VJ, Meuli R, Thiran JP. Mapping human whole-brain structural networks with diffusion MRI. PloS one. 2007; 2(7):e597. [PubMed: 17611629]

Hall M, Frank E, Holmes G, Pfahringer B, Reutemann P, Witten IH. The WEKA data mining software: an update. ACM SIGKDD Explorations Newsletter. 2009; 11(1):10–18.

Hanaie R, Mohri I, Kagitani-Shimono K, Tachibana M, Azuma J, Matsuzaki J, Watanabe Y, Fujita N, Taniike M. Altered microstructural connectivity of the superior cerebellar peduncle is related to

motor dysfunction in children with autistic spectrum disorders. The Cerebellum. 2013; 12(5):645–656. DOI: 10.1007/s12311-013-0475-x [PubMed: 23564050]

Hao X, Zygmunt K, Whitaker RT, Fletcher PT. Improved segmentation of white matter tracts with adaptive Riemannian metrics. Medical Image Analysis. 2014; 18(1):161–175. [PubMed: 24211814]

Hess CP, Mukherjee P, Han ET, Xu D, Vigneron DB. Q-ball reconstruction of multimodal fiber orientations using the spherical harmonic basis. Magnetic Resonance in Medicine. 2006; 56(1): 104–117. DOI: 10.1002/mrm.20931 [PubMed: 16755539]

Clemm von Hohenberg C, Schocke M, Wigand M, Nachbauer W, Guttmann C, Kubicki M, Shenton M, Boesch S, Egger K. Radial diffusivity in the cerebellar peduncles correlates with clinical severity in Friedreich ataxia. Neurological Sciences. 2013; 34(8):1459–1462. DOI: 10.1007/s10072-013-1402-0 [PubMed: 23640016]

Hüttlova J, Kikinis Z, Kerkovsky M, Bouix S, Vu MA, Makris N, Shenton M, Kasparek T. Abnormalities in myelination of the superior cerebellar peduncle in patients with schizophrenia and deficits in movement sequencing. The Cerebellum. 2014; :1–10. DOI: 10.1007/s12311-014-0550-y [PubMed: 23925594]

Knutsson H. Producing a continuous and distance preserving 5-D vector representation of 3-D orientation. IEEE Computer Society Workshop on Computer Architecture for Pattern Analysis and Image Database Management. 1985; :175–182. DOI: 10.1109/ISBI.2010.5490203

Landman BA, Farrell JAD, Patel NL, Mori S, Prince JL. DTI fiber tracking: the importance of adjusting DTI gradient tables for motion correction. CATNAP – a tool to simplify and accelerate DTI analysis. Proc Org Human Brain Mapping 13th Annual Meeting. 2007

Landman BA, Bogovic JA, Wan H, ElShahaby FEZ, Bazin PL, Prince JL. Resolution of crossing fibers with constrained compressed sensing using diffusion tensor MRI. NeuroImage. 2012; 59(3):2175–2186. [PubMed: 22019877]

Lawes INC, Barrick TR, Murugam V, Spierings N, Evans DR, Song M, Clark CA. Atlas-based segmentation of white matter tracts of the human brain using diffusion tensor tractography and comparison with classical dissection. NeuroImage. 2008; 39(1):62–79. [PubMed: 17919935]

Le Bihan D, Mangin JF, Poupon C, Clark CA, Pappata S, Molko N, Chabriat H. Diffusion tensor imaging: concepts and applications. Journal of Magnetic Resonance Imaging. 2001; 13(4):534–546. [PubMed: 11276097]

Lenglet C, Rousson M, Deriche R. DTI segmentation by statistical surface evolution. IEEE Transactions on Medical Imaging. 2006; 25(6):685–700. [PubMed: 16768234]

Lucas BC, Bogovic JA, Carass A, Bazin PL, Prince JL, Pham DL, Landman BA. The Java image science toolkit (JIST) for rapid prototyping and publishing of neuroimaging software. Neuroinformatics. 2010; 8(1):5–17. [PubMed: 20077162]

Maddah M, Mewes AUJ, Haker S, Grimson WEL, Warfield SK. Automated atlas-based clustering of white matter fiber tracts from DTMRI. Medical Image Computing and Computer-Assisted Intervention–MICCAI, 2005. 2005; 3749:188–195.

Maddah M, Grimson WEL, Warfield SK, Wells WM. A unified framework for clustering and quantitative analysis of white matter fiber tracts. Medical Image Analysis. 2008; 12(2):191–202. DOI: 10.1016/j.media.2007.10.003 [PubMed: 18180197]

Malcolm JG, Michailovich O, Bouix S, Westin CF, Shenton ME, Rathi Y. A filtered approach to neural tractography using the Watson directional function. Medical Image Analysis. 2010; 14(1):58–69. [PubMed: 19914856]

Michailovich O, Rathi Y, Dolui S. Spatially regularized compressed sensing for high angular resolution diffusion imaging. IEEE Transactions on Medical Imaging. 2011; 30(5):1100–1115. [PubMed: 21536524]

Mori, S.; Wakana, S.; van Zijl, PCM.; Nagae-Poetscher, LM. MRI Atlas of Human White Matter, First Edition. Elsevier Science; 2005.

Murata Y, Kawakami H, Yamaguchi S, Nishimura M, Kohriyama T, Ishizaki F, Matsuyama Z, Mimori Y, Nakamura S. Characteristic magnetic resonance imaging findings in spinocerebellar ataxia 6. Archives of Neurology. 1998; 55(10):1348. [PubMed: 9779664]

Nicoletti G, Fera F, Condino F, Auteri W, Gallo O, Pugliese P, Arabia G, Morgante L, Barone P, Zappia M, Quattrone A. MR imaging of middle cerebellar peduncle width: Differentiation of multiple system atrophy from Parkinson disease. Radiology. 2006; 239(3):825–830. [PubMed: 16714464]

Nolte, J. The Human Brain: An Introduction to Its Functional Anatomy. Mosby; 2002.

O'Donnell LJ, Westin CF. Automatic tractography segmentation using a high-dimensional white matter atlas. IEEE Transactions on Medical Imaging. 2007; 26(11):1562–1575. [PubMed: 18041271]

O'Donnell LJ, Kubicki M, Shenton ME, Dreusicke MH, Grimson WEL, Westin CF. A method for clustering white matter fiber tracts. American Journal of Neuroradiology. 2006; 27(5):1032–1036. http://www.ajnr.org/content/27/5/1032.full.pdf+html. [PubMed: 16687538]

Oishi K, Mori S, Donohue PK, Ernst T, Anderson L, Buchthal S, Faria A, Jiang H, Li X, Miller MI, van Zijl PC, Chang L. Multi-contrast human neonatal brain atlas: application to normal neonate development analysis. NeuroImage. 2011; 56(1):8–20. [PubMed: 21276861]

Ojemann JG, Partridge SC, Poliakov AV, Niazi TN, Shaw DW, Ishak GE, Lee A, Browd SR, Geyer J, Ellenbogen RG. Diffusion tensor imaging of the superior cerebellar peduncle identifies patients with posterior fossa syndrome. Child's Nervous System. 2013; 29(11):2071–2077. DOI: 10.1007/s00381-013-2205-6

Peled S, Friman O, Jolesz F, Westin CF. Geometrically constrained two-tensor model for crossing tracts in DWI. Magnetic Resonance Imaging. 2006; 24(9):1263–1270. [PubMed: 17071347]

Perrini P, Tiezzi G, Castagna M, Vannozzi R. Three-dimensional microsurgical anatomy of cerebellar peduncles. Neurosurgical Review. 2012:1–11.

Qazi AA, Radmanesh A, O'Donnell L, Kindlmann G, Peled S, Whalen S, Westin CF, Golby AJ. Resolving crossings in the corticospinal tract by two-tensor streamline tractography: Method and clinical assessment using fMRI. NeuroImage. 2009; 47:98–106. [PubMed: 19361567]

Ramirez-Manzanares A, Rivera M, Vemuri BC, Carney P, Mareci T. Diffusion basis functions decomposition for estimating white matter intravoxel fiber geometry. IEEE Transactions on Medical Imaging. 2007; 26(8):1091–1102. [PubMed: 17695129]

Sinke RJ, Ippel EF, Diepstraten CM, Beemer FA, Wokke JH, van Hilten BJ, Knoers NV, van Amstel HKP, Kremer H. Clinical and molecular correlations in spinocerebellar ataxia type 6: a study of 24 Dutch families. Archives of Neurology. 2001; 58(11):1839. [PubMed: 11708993]

Sivaswamy L, Kumar A, Rajan D, Behen M, Muzik O, Chugani D, Chugani H. A diffusion tensor imaging study of the cerebellar pathways in children with autism spectrum disorder. Journal of Child Neurology. 2010; 25(10):1223–1231. [PubMed: 20179000]

Suarez RO, Commowick O, Prabhu SP, Warfield SK. Automated delineation of white matter fiber tracts with a multiple region-of-interest approach. NeuroImage. 2012; 59(4):3690–3700. DOI: 10.1016/j.neuroimage.2011.11.043 [PubMed: 22155046]

Tournier JD, Calamante F, Connelly A. Robust determination of the fibre orientation distribution in diffusion MRI: Non-negativity constrained super-resolved spherical deconvolution. NeuroImage. 2007; 35(4):1459–1472. [PubMed: 17379540]

Tuch DS. Q-ball imaging. Magnetic Resonance in Medicine. 2004; 52(6):1358–1372. DOI: 10.1002/mrm.20279 [PubMed: 15562495]

Tuch DS, Reese TG, Wiegell MR, Makris N, Belliveau JW, Wedeen VJ. High angular resolution diffusion imaging reveals intravoxel white matter fiber heterogeneity. Magnetic Resonance in Medicine. 2002; 48(4):577–582. DOI: 10.1002/mrm.10268 [PubMed: 12353272]

Wang F, Sun Z, Du X, Wang X, Cong Z, Zhang H, Zhang D, Hong N. A diffusion tensor imaging study of middle and superior cerebellar peduncle in male patients with schizophrenia. Neuroscience Letters. 2003; 348(3):135–138. [PubMed: 12932812]

Wang S, Fan GG, Xu K, Wang C. Altered microstructural connectivity of the superior and middle cerebellar peduncles are related to motor dysfunction in children with diffuse periventricular leucomalacia born preterm: A DTI tractography study. European Journal of Radiology. 2014; 83(6):997–1004. DOI http://dx.doi.org/10.1016/j.ejrad.2014.03.010. [PubMed: 24703518]

Wang X, Grimson WEL, Westin CF. Tractography segmentation using a hierarchical Dirichlet processes mixture model. NeuroImage. 2011; 54(1):290–302. [PubMed: 20678578]

Wang Z, Vemuri BC. DTI segmentation using an information theoretic tensor dissimilarity measure. IEEE Transactions on Medical Imaging. 2005; 24(10):1267–1277. [PubMed: 16229414]

Warfield SK, Zou KH, Wells WM. Simultaneous truth and performance level estimation (STAPLE): an algorithm for the validation of image segmentation. IEEE Transactions on Medical Imaging. 2004; 23(7):903–921. [PubMed: 15250643]

Wedeen VJ, Hagmann P, Tseng WYI, Reese TG, Weisskoff RM. Mapping complex tissue architecture with diffusion spectrum magnetic resonance imaging. Magnetic Resonance in Medicine. 2005; 54(6):1377–1386. DOI: 10.1002/mrm.20642 [PubMed: 16247738]

Westin CF, Peled S, Gudbjartsson H, Kikinis R, Jolesz FA. Geometrical diffusion measures for MRI from tensor basis analysis. Proceedings of ISMRM. 1997; 97:1742.

Xu C, Yezzi A Jr, Prince JL. On the relationship between parametric and geometric active contours. IEEE Conference Record of the Thirty-Fourth Asilomar Conference on Signals, Systems and Computers, 2000. 2000; 1:483–489.

Ye C, Bazin PL, Bogovic JA, Ying SH, Prince JL. Labeling of the cerebellar peduncles using a supervised Gaussian classifier with volumetric tract segmentation. Proceedings of SPIE Medical Imaging. 2012; 8314:143.

Ye C, Bogovic JA, Ying SH, Prince JL. Segmentation of the complete superior cerebellar peduncles using a multi-object geometric deformable model. 2013 IEEE 10th International Symposium on Biomedical Imaging (ISBI). 2013:49–52.

Ying SH, Landman BA, Chowdhury S, Sinofsky AH, Gambini A, Mori S, Zee DS, Prince JL. Orthogonal diffusion-weighted MRI measures distinguish region-specific degeneration in cerebellar ataxia subtypes. Journal of Neurology. 2009; 256(11):1939–1942. [PubMed: 19653028]

Yushkevich PA, Zhang H, Simon TJ, Gee JC. Structure-specific statistical mapping of white matter tracts. NeuroImage. 2008; 41(2):448–461. [PubMed: 18407524]

Zhang H, Avants BB, Yushkevich PA, Woo JH, Wang S, McCluskey LF, Elman LB, Melhem ER, Gee JC. High-dimensional spatial normalization of diffusion tensor images improves the detection of white matter differences: an example study using amyotrophic lateral sclerosis. IEEE Transactions on Medical Imaging. 2007; 26(11):1585–1597. [PubMed: 18041273]

Zhang S, Correia S, Laidlaw DH. Identifying white-matter fiber bundles in DTI data using an automated proximity-based fiber-clustering method. IEEE Transactions on Visualization and Computer Graphics. 2008; 14(5):1044–1053. DOI: 10.1109/TVCG.2008.52 [PubMed: 18599916]

Zhou Q, Michailovich O, Rathi Y. Resolving complex fibre architecture by means of sparse spherical deconvolution in the presence of isotropic diffusion. SPIE Medical Imaging, International Society for Optics and Photonics. 2014:903,425–903,425.

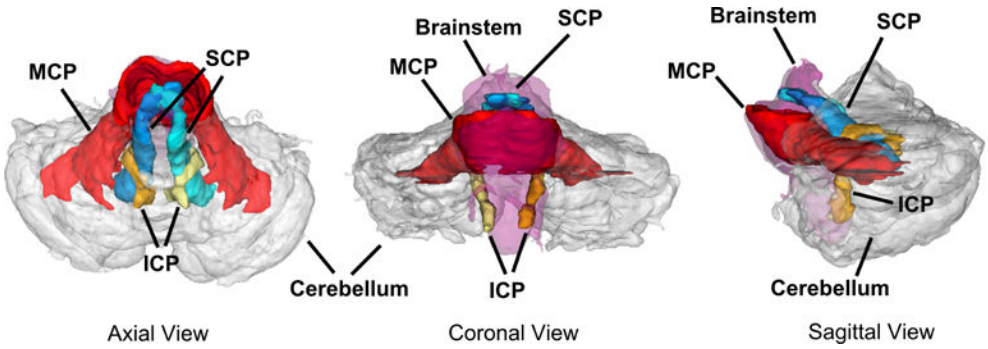

Fig. 1.

A manually drawn schematic of the cerebellar peduncles. Blue: left SCP; green: right SCP; red: MCP; orange: left ICP; yellow: right ICP. Shown together with the cerebellum (gray) and the brainstem (purple)

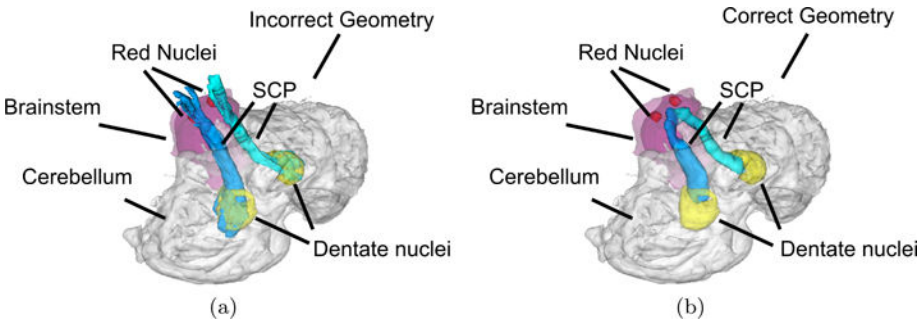

Fig. 2.

The SCPs (blue and green) shown with the red nuclei (red) and the dentate nuclei (yellow): (a) typical incorrect SCPs obtained from DTI and (b) segmentation of the SCPs including the decussation in the proposed method. Note that our SCPs do not extend through the dentate nuclei, which leads to a different appearance of the dentate nuclei due to transparency

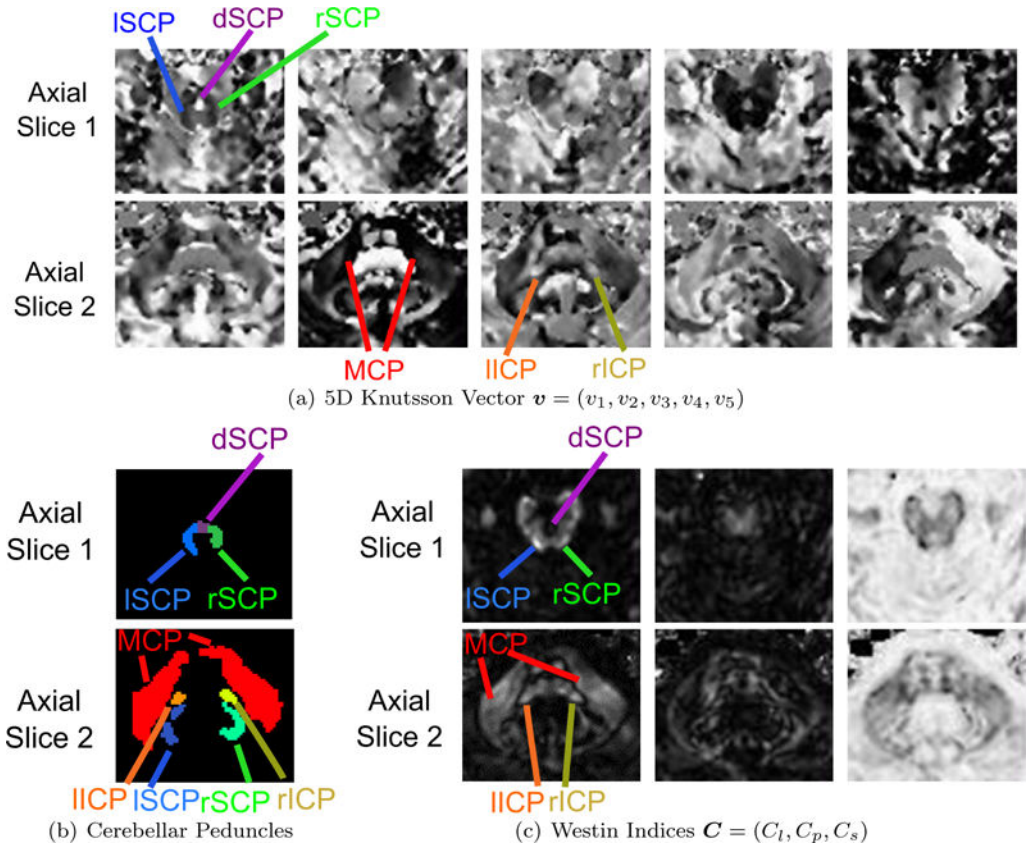

Fig. 3.

Diffusion properties and cerebellar peduncles on two representative slices (Row 1 and 2 in each subfigure): (a) the 5D Knutsson vector, (b) the cerebellar peduncles for reference, and (c) the Westin indices. Within each subfigure, Row 1 shows an axial slice cutting through the brainstem where the SCPs decussate, and Row 2 shows an axial slice cutting through the body of the MCP

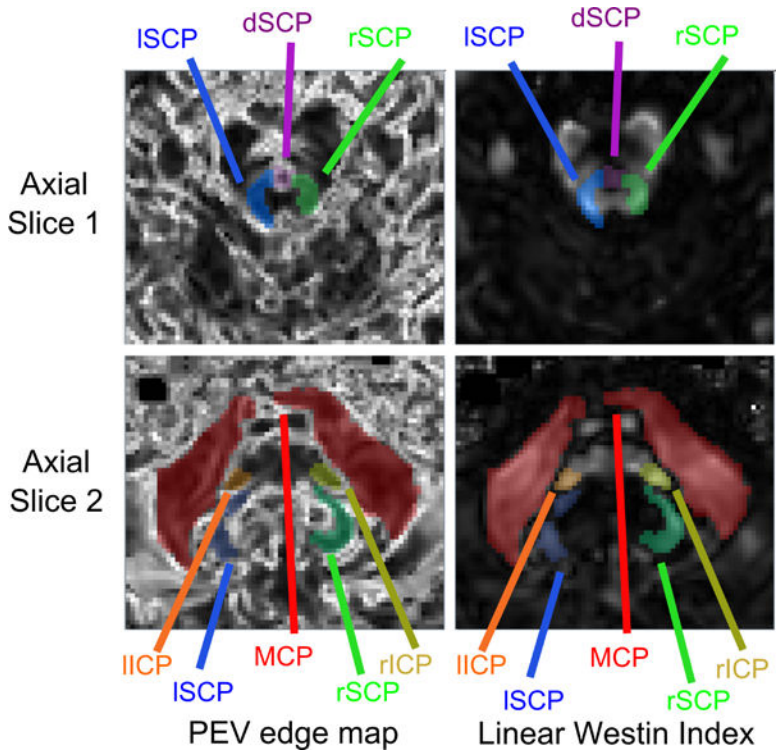

Fig. 4.

Manual delineations of the cerebellar peduncles overlaid on the PEV edge map (left) and the C_l map (right) on two representative slices (Row 1 and 2) in correspondence with Fig. 3. Row 1 shows an axial slice cutting through the brainstem where the SCPs decussate, and Row 2 shows an axial slice cutting through the body of the MCP

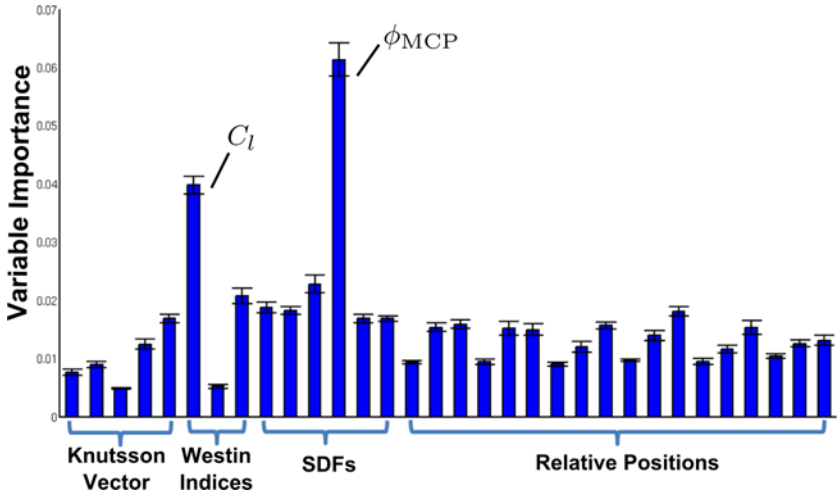

Fig. 5.

Means and standard deviations of the variable importance in the cross-validation test. The order of the variables is the same as in the feature vector $\boldsymbol{f} = (\boldsymbol{v}, \boldsymbol{C}, \varphi, \boldsymbol{x})$

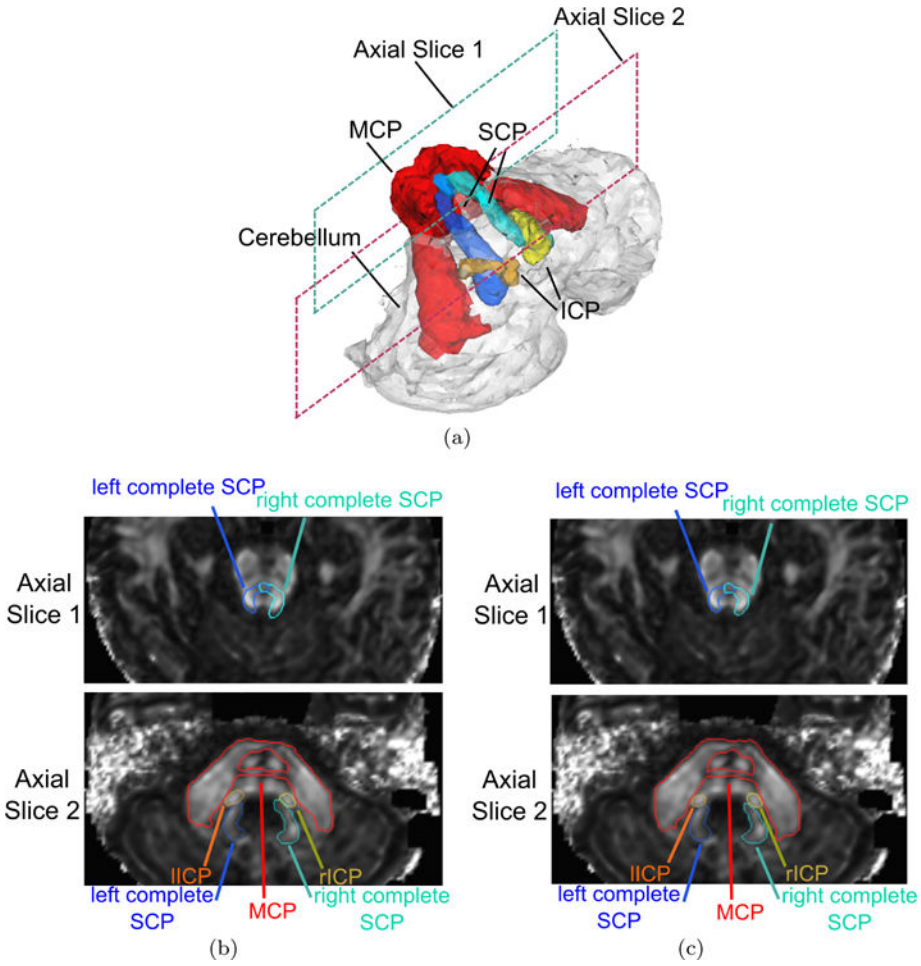

Fig. 6.

A segmentation result. (a) A 3D rendering (oblique view) of the cerebellar peduncles segmented by the proposed method in the cross-validation test, shown together with the cerebellum (gray). Axial cross sections of (b) the manual delineations and (c) the proposed segmentation contours overlaid on the FA map. Slice 1: a cut through the brainstem where the SCPs decussate. Slice 2: a cut through the cerebellum where all the cerebellar peduncles are visible. In all figures here, the left and right noncrossing SCPs are combined respectively with the dSCP to obtain the complete left and right SCPs. Blue: left complete SCP; green: right complete SCP; red: MCP; orange: lICP; yellow: rICP

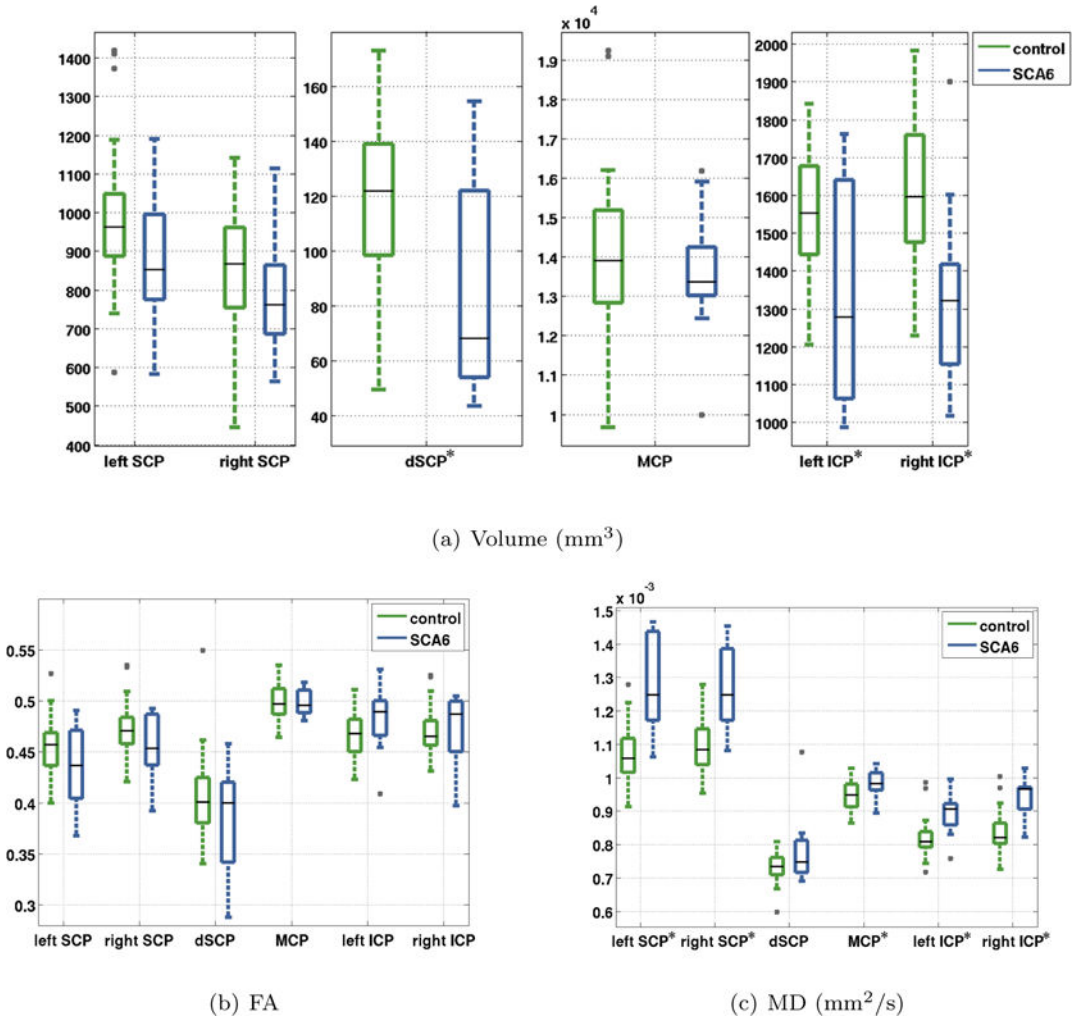

Fig. 7.

Box plots of (a) tract volumes, (b) average FAs, and (c) average MDs of the segmented cerebellar peduncles. The numbers are compared between the control and the SCA6 group. Asterisks (*) indicate that statistically significant difference ($p < 0.05$) is observed in both the Student's *t*-test and the Wilcoxon rank-sum test

Table 1

The Dice coefficients between the segmentation results and manual delineations. Mean Dice coefficients from the proposed method are set in bold font

	RFC						RFC+MGDM					
	lSCP	**rSCP**	**dSCP**	**MCP**	**lICP**	**rICP**	**lSCP**	**rSCP**	**dSCP**	**MCP**	**lICP**	**rICP**
S1	0.828	0.793	0.702	0.826	0.753	0.762	0.839	0.762	0.689	0.817	0.782	0.787
S2	0.776	0.766	0.753	0.860	0.670	0.660	0.824	0.816	0.815	0.850	0.675	0.676
S3	0.774	0.722	0.834	0.831	0.712	0.710	0.803	0.783	0.870	0.828	0.759	0.752
S4	0.739	0.797	0.719	0.874	0.655	0.616	0.815	0.809	0.758	0.870	0.695	0.648
S5	0.820	0.797	0.816	0.856	0.777	0.728	0.798	0.775	0.862	0.864	0.777	0.778
S6	0.813	0.778	0.286	0.838	0.678	0.689	0.786	0.770	0.711	0.843	0.704	0.729
S7	0.833	0.820	0.755	0.865	0.720	0.680	0.769	0.795	0.775	0.872	0.731	0.702
S8	0.807	0.785	0.826	0.829	0.640	0.668	0.785	0.767	0.785	0.851	0.681	0.705
S9	0.785	0.763	0.787	0.851	0.739	0.674	0.799	0.795	0.833	0.855	0.765	0.707
Mean	0.797	0.780	0.720	0.848	0.705	0.688	**0.802**	**0.786**	**0.789**	**0.850**	**0.730**	**0.720**
Std.	0.031	0.028	0.169	0.017	0.047	0.042	0.022	0.019	0.063	0.018	0.042	0.046

	SyN+s-STAPLE						DTI-TK+s-STAPLE					
	lSCP	**rSCP**	**dSCP**	**MCP**	**lICP**	**rICP**	**lSCP**	**rSCP**	**dSCP**	**MCP**	**lICP**	**rICP**
S1	0.748	0.693	0.637	0.832	0.732	0.773	0.784	0.770	0.725	0.819	0.751	0.757
S2	0.793	0.797	0.704	0.852	0.625	0.657	0.803	0.799	0.746	0.839	0.672	0.683
S3	0.731	0.757	0.794	0.815	0.715	0.622	0.724	0.726	0.597	0.813	0.764	0.692
S4	0.804	0.771	0.764	0.865	0.729	0.662	0.796	0.780	0.585	0.852	0.753	0.694
S5	0.721	0.697	0.752	0.856	0.705	0.728	0.803	0.770	0.741	0.832	0.737	0.727
S6	0.689	0.750	0.528	0.853	0.662	0.723	0.686	0.725	0.563	0.853	0.648	0.682
S7	0.709	0.753	0.640	0.848	0.637	0.678	0.748	0.748	0.571	0.835	0.625	0.651
S8	0.753	0.697	0.618	0.814	0.675	0.672	0.765	0.754	0.630	0.790	0.634	0.586
S9	0.764	0.774	0.836	0.838	0.746	0.742	0.758	0.770	0.817	0.814	0.710	0.725
Mean	0.746	0.744	0.697	0.841	0.692	0.695	0.763	0.760	0.664	0.828	0.699	0.689
Std.	0.038	0.038	0.099	0.018	0.044	0.048	0.039	0.025	0.094	0.020	0.055	0.049

Table 2

The ASDs (mm) between the segmentation results and manual delineations. The mean ASDs from the proposed method are set in bold font

	RFC						RFC+MGDM					
	lSCP	**rSCP**	**dSCP**	**MCP**	**lICP**	**rICP**	**lSCP**	**rSCP**	**dSCP**	**MCP**	**lICP**	**rICP**
S1	0.391	0.562	0.484	0.618	0.647	0.561	0.408	0.675	0.552	0.700	0.582	0.523
S2	0.621	0.627	0.385	0.542	0.895	0.816	0.501	0.510	0.298	0.599	0.902	0.796
S3	0.585	0.748	0.314	0.621	0.700	0.676	0.521	0.590	0.268	0.663	0.611	0.614
S4	0.591	0.452	0.423	0.504	0.826	0.893	0.424	0.449	0.358	0.551	0.797	0.873
S5	0.820	0.797	0.816	0.856	0.777	0.728	0.512	0.539	0.212	0.569	0.589	0.516
S6	0.416	0.486	0.945	0.801	0.776	0.723	0.492	0.552	0.395	0.789	0.735	0.635
S7	0.354	0.377	0.275	0.734	0.645	0.813	0.533	0.503	0.313	0.678	0.641	0.755
S8	0.430	0.456	0.234	0.846	0.876	0.785	0.518	0.543	0.291	0.759	0.819	0.710
S9	0.450	0.516	0.376	0.720	0.635	0.801	0.458	0.471	0.328	0.684	0.596	0.725
Mean	0.518	0.558	0.472	0.694	0.753	0.755	**0.485**	**0.537**	**0.335**	**0.666**	**0.697**	**0.683**
Std.	0.149	0.141	0.246	0.129	0.101	0.097	0.045	0.067	0.097	0.081	0.119	0.121

	SyN+s-STAPLE						DTI-TK+s-STAPLE					
	lSCP	**rSCP**	**dSCP**	**MCP**	**lICP**	**rICP**	**lSCP**	**rSCP**	**dSCP**	**MCP**	**lICP**	**rICP**
S1	0.669	0.827	0.684	0.614	0.691	0.540	0.519	0.612	0.463	0.690	0.633	0.583
S2	0.547	0.534	0.562	0.611	1.089	0.984	0.527	0.517	0.388	0.730	0.854	0.739
S3	0.711	0.638	0.400	0.684	0.761	1.183	0.711	0.679	0.772	0.685	0.604	0.842
S4	0.558	0.540	0.411	0.541	0.618	0.810	0.786	0.515	0.571	0.590	0.577	0.704
S5	0.698	0.743	0.386	0.587	0.843	0.698	0.481	0.540	0.350	0.664	0.673	0.677
S6	0.782	0.607	0.831	0.624	0.737	0.657	0.793	0.686	0.787	0.662	0.795	0.706
S7	0.786	0.614	0.568	0.899	0.909	0.803	0.585	0.578	0.640	0.998	0.926	0.835
S8	0.595	0.764	0.630	1.042	0.764	0.770	0.531	0.564	0.567	1.168	0.870	1.003
S9	0.593	0.533	0.309	0.963	0.641	0.655	0.629	0.526	0.314	1.047	0.724	0.675
Mean	0.660	0.645	0.531	0.729	0.784	0.789	0.618	0.580	0.539	0.804	0.740	0.752
Std.	0.091	0.109	0.169	0.186	0.146	0.194	0.119	0.066	0.174	0.208	0.127	0.124

Table 3

The *p*-values of the paired Student's *t*-test and the Wilcoxon signed-rank test for comparing the Dice coefficients between RFC + MGDM results and the other three results. Note that the mean Dice coefficients of RFC + MGDM are greater than those in the other three results as shown in Table 1

	Paired Student's *t*-test					
	lSCP	**rSCP**	**dSCP**	**MCP**	**lICP**	**rICP**
RFC	0.7520	0.6341	0.1726	0.5317	0.0019 *	1.4E-5 ***
SyN + s-STAPLE	0.0005 ***	0.0007 ***	0.0037 *	0.1521	0.0161 *	0.1424
DTI-TK + s-STAPLE	0.0080 *	0.0071 *	0.0044 *	0.0162 *	0.0834	0.0882

	Wilcoxon signed-rank test					
	lSCP	**rSCP**	**dSCP**	**MCP**	**lICP**	**rICP**
RFC	0.8203	0.7344	0.0547	0.6523	0.0039 *	0.0039 *
SyN + s-STAPLE	0.0039 *	0.0039 *	0.0195 *	0.2031	0.0195 *	0.1641
DTI-TK + s-STAPLE	0.0078 *	0.0117 *	0.0117 *	0.0195 *	0.1641	0.0742

Note:

* $p < 0.05$,

*** $p < 0.001$

Table 4

The *p*-values of the paired Student's *t*-test and the Wilcoxon signed-rank test for comparing the ASDs between RFC + MGDM results and the other three results. Note that the mean ASDs in RFC + MGDM results are lower than those in the other three results as shown in Table 2

	Paired Student's *t*-test					
	lSCP	**rSCP**	**dSCP**	**MCP**	**lICP**	**rICP**
RFC	0.5339	0.6506	0.1458	0.4810	0.0190 *	0.0057 *
SyN + s-STAPLE	0.0003 ***	0.0018 *	0.0033 *	0.2686	0.1160	0.1430
DTI-TK + s-STAPLE	0.0184 *	0.0571	0.0130 *	0.0560	0.3740	0.1970

	Wilcoxon signed-rank test					
	lSCP	**rSCP**	**dSCP**	**MCP**	**lICP**	**rICP**
RFC	0.8203	0.7344	0.2031	0.8203	0.0117 *	0.0039 *
SyN + s-STAPLE	0.0039 *	0.0039 *	0.0078 *	0.2500	0.1289	0.2031
DTI-TK + s-STAPLE	0.0195 *	0.0391 *	0.0195 *	0.0547	0.2031	0.1641

Note:

* $p < 0.05$,

*** $p < 0.001$

Table 5

The *p*-values of the Student's *t*-test and the Wilcoxon rank-sum test for comparing the volumes, average FAs, and average MDs of the cerebellar peduncles between the control and SCA6 group

Volume

	lSCP	rSCP	dSCP	MCP	lICP	rICP
Student's *t*-test	0.0857	0.2902	0.0321 *	0.3737	0.0465 *	0.0055 *
Wilcoxon rank-sum test	0.0977	0.1517	0.0269 *	0.5683	0.0466 *	0.0013 *

FA

	lSCP	rSCP	dSCP	MCP	lICP	rICP
Student's *t*-test	0.2089	0.1335	0.2344	0.9134	0.1576	0.7310
Wilcoxon rank-sum test	0.3806	0.2596	0.4276	0.9889	0.0466 *	0.4116

MD

	lSCP	rSCP	dSCP	MCP	lICP	rICP
Student's *t*-test	0.0005 ***	0.0010 *	0.1476	0.0262 *	0.0028 *	0.0002 ***
Wilcoxon rank-sum test	0.0001 ***	0.0002 ***	0.2368	0.0332 *	0.0014 *	0.0002 ***

Note:

* $p < 0.05$,

*** $p < 0.001$

Table 6

Partial volume fraction for the control subjects and SCA6 patients in the data set used in Section 3.2

	Control						SCA6					
	lSCP	**rSCP**	**dSCP**	**MCP**	**lICP**	**rICP**	**lSCP**	**rSCP**	**dSCP**	**MCP**	**lICP**	**rICP**
Mean	0.509	0.506	0.677	0.340	0.509	0.514	0.518	0.524	0.775	0.334	0.574	0.575
Std.	0.032	0.029	0.067	0.018	0.029	0.024	0.040	0.050	0.103	0.017	0.050	0.057